metals

MDPI

Article

Fracture Mechanics Modeling of Fatigue Behaviors of Adhesive-Bonded Aluminum Alloy Components

Yuning Zhang [1], Pingsha Dong [1,*] and Xianjun Pei [2]

[1] Department of Naval Architecture and Marine Engineering, University of Michigan, Ann Arbor, MI 48109, USA; zyuning@umich.edu
[2] School of Mechanical Engineering, Southeast University, Nanjing 211189, China; xpei@seu.edu.cn
* Correspondence: dongp@umich.edu; Tel.: +1-734-615-7487

Abstract: Adhesive-bonding has become increasingly adopted for multi-material lightweight applications (e.g., automotive structures). There is a growing interest in understanding the fatigue behaviors in this type of joint for supporting structural durability modeling in practice. In this paper, an analytical fracture mechanics modeling procedure is presented in the context of a generalized sandwich specimen. Its closed form stress intensity factor solutions were then derived and applied for the correlating fatigue test data obtained from the lap-shear and coach-peel test specimens with demonstrated effectiveness. Some important implications of these analytical solutions on joint design are also discussed.

Keywords: fracture mechanics modeling; stress intensity factor; fatigue; adhesive joint; aluminum alloy

Citation: Zhang, Y.; Dong, P.; Pei, X. Fracture Mechanics Modeling of Fatigue Behaviors of Adhesive-Bonded Aluminum Alloy Components. *Metals* **2022**, *12*, 1298. https://doi.org/10.3390/met12081298

Academic Editor: Koji Takahashi

Received: 29 June 2022
Accepted: 29 July 2022
Published: 1 August 2022

1. Introduction

Multi-material structures have become a major trend in the future transportation systems for achieving effective light-weight and smart functionalities [1–3]. In addition to new dissimilar materials joining methods [4–9] that are currently under development, adhesive bonding offers reliable and convenient solutions [10]. However, structural durability modeling of adhesive joints for vehicle development has been a major challenge to meet today's rapid virtual prototyping needs, as discussed in [4,7]. This is mainly due to the fact that the stress state governing fatigue in adhesive joints is more complex than that in welded joints due to the significant mismatch in the mechanical properties between the adhesive and adherends. Most of the studies in the literature to date has been focused on either developing empirical methods through selected durability testing for supporting product development [11,12], which can introduce uncertainties in actual applications, or establish effective fundamental mechanics-based models, most of which remain difficult to be readily used for structural applications [13,14].

The existing investigations, particularly for those relevant to automotive applications, can be characterized into a few categories. The first category is the experimental approach through performing the testing of joint static strengths and/or joint fatigue properties [1,15–19] by focusing on joint geometry, specimen type, load level, or the load ratio effects on the fatigue behaviors. As discussed in [5], it is difficult to relate the joint static strength to fatigue performance even in an empirical sense, since the former is relatively less sensitive to stress concentration while the latter is governed by joint stress concentration behaviors. As far as fatigue testing using simple specimen types (e.g., lap-shear and coach-peel) is concerned, one unresolved issue is how to make use of the raw test data in terms of the nominal stress or strain versus cycle to failure to the joint fatigue properties that can be used as the input to the computational model of structures.

The second category can be characterized as continuum mechanics-based modeling approach by focusing on a detailed stress state in adhesive joints either through finite element methods or idealized analytical models. This approach offers the advantages of

gaining mechanical insights that can be translated to broader applications. Representative publications along this line are the shear lag model by Volkersen [13], by assuming elastic shear deformation in the adhesive layer and elastic tension deformation in the adherend layers, and a single lap joint model by Goland and Reissner [14], by incorporating the bending moment due to an eccentrically applied load. These two types of models represent the classical one dimensional (1D) linear elastic approach. Their further improvements can be found [20–35] by considering the 2D, and even 3D effects as well as the geometric and material nonlinearity. For the latter cases, the solutions are often only attenable through finite element methods. As a result, most of the solutions in this category exhibit some level of mesh-size sensitivity, therefore introducing some uncertainties at geometric discontinuity locations in which the stress or strain singularity typically exists when sharp corners or notches are present.

The third approach is fracture mechanics modeling by computing a fracture mechanics parameter directly such as the stress intensity factor or energy release rate, which can then be related to the joint fatigue behaviors. Dillard [36] summarized how the fracture mechanics were developed and applied to the adhesive joint. Recently, Chen et al. [1] analyzed the geometry influence on the fatigue performance by computing the well-established J integral (i.e., energy release rate) of the lap-shear and coach-peel specimens of the adhesive-bonded aluminum alloy joints. When assuming a pre-determined initial crack size, the results seemed to show some promise in their test data correlation. However, the pre-determined initial crack size has to be determined through experimental testing, which can introduce uncertainties. As a result, the generality of the approach requires further study.

Cohesive zone model (CZM) is another popular analysis method that many researchers are using to evaluate fatigue behavior [37–39]. This method avoids the stress singularity problem and can numerically predict fatigue life, and the probabilistic method is sometimes used to achieve a faster calculation speed than the FE method [37,38], but too many parameters need to be calibrated to have a good result.

In this paper, we present an analytical approach by considering a general sandwich specimen containing an adhesive layer subjected to a set of simple loading conditions, on which closed form stress intensity factors can be developed. Through a linear superposition, we show that the stress intensity factors for typical lap-shear and coach-peel specimens can be obtained in closed forms and validated by finite element solutions. Then, the fatigue test data obtained on the lap-shear and coach-peel specimens made of aluminum-to-aluminum adhesive joints are shown to be effectively correlated into a narrow band in the form of an effective stress intensity factor range versus cycles to failure. Insights offered by the analytical solutions on the joint design parameters will also be discussed in light of the present study.

2. Analytical Fracture Mechanics Modeling

2.1. Problem Idealization

Two commonly used fatigue test specimen types (e.g., coach-peel and lap-shear [1,40]), are illustrated in Figure 1. The corresponding mechanical behaviors can be modeled by considering a general sandwich model, as shown in Figure 2, in which f_1 through f_4 represent the boundary normal tractions measured in force per unit length in x; v_1 through v_4 are the boundary transverse shear tractions; and m_1 through m_4 are the moment tractions measured in moment per unit length in z. To facilitate the development of closed-form solutions, it was assumed that the two adherends had the same thickness (i.e., $t_1 = t_2 = t$), while the adhesive thickness was represented as t_a.

With the descriptions given in Figure 2, the coach-peel specimen illustrated in Figure 1a can be represented by setting all tractions being zero, except that $m_1 = -m_2 = m_0$ and $v_1 = -v_2 = v_0$, as shown in Figure 3a. Through a comparison with Figure 1a, m_0 and v_0 can be related to remote loading as Fc/W and F/W, respectively, where W is the width of the specimen or the width into paper. Note that L in Figure 2 is the bond length. The stress analysis problem associated with the coach-peel specimen shown in Figure 1a is now

reduced to the problem described as Case 1 in Figure 3a, which possesses symmetry with respect to the mid-thickness of the adhesive layer.

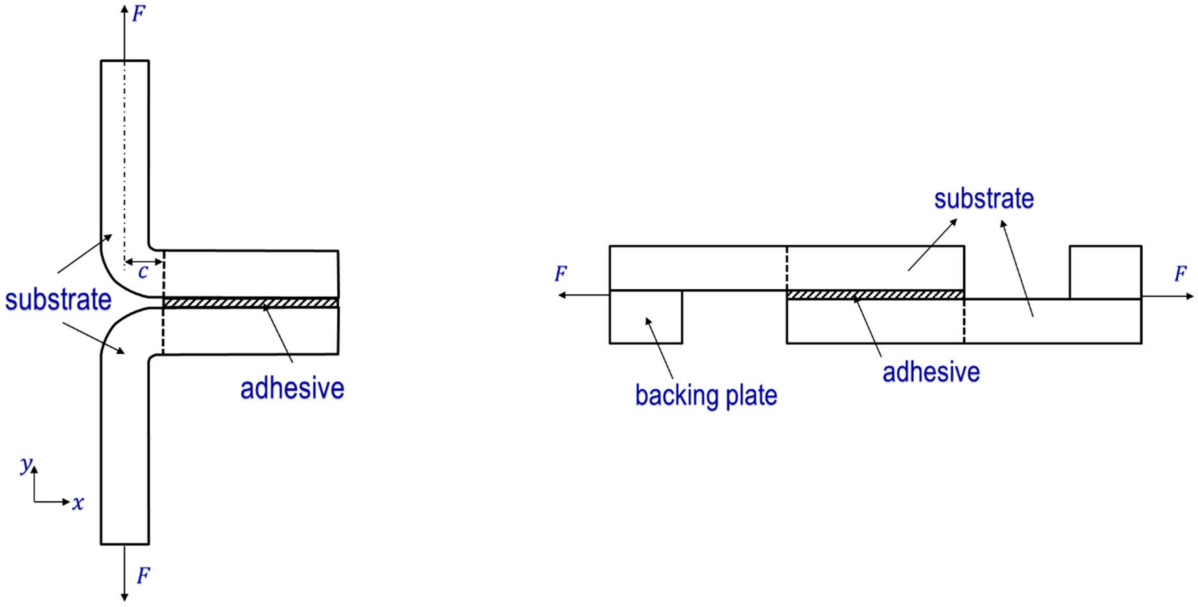

(**a**) (**b**)

Figure 1. Two commonly used fatigue test specimens for adhesive joints. (**a**) Coach-peel. (**b**) Lap-shear.

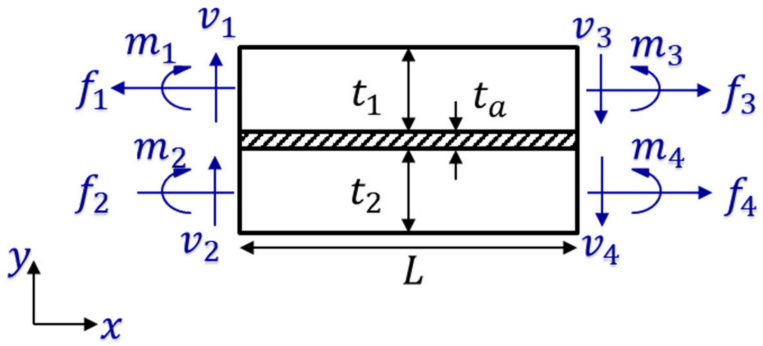

Figure 2. A sandwich model representation of the bonded section.

Similarly, the typical lap-shear test specimen shown in Figure 1b can be represented by non-zero $f_1 = f_4 = f_0$, and $m_1 = -m_4 = m_0$, which can be further decomposed into three subcases within which Case 0 has no contribution to the crack driving force (e.g., stress intensity factor) with respect to a hypothetical crack situated in the mid-thickness of the adhesive layer. Case 2 is under the pure moment loading, acting symmetrically with respect to both coordinate axes, while Case 3 represents the anti-symmetric loading with respect to both coordinate axes. As such, Case 2 contributes the Mode I stress intensity factor (K_I) with respect to a crack situated in the mid thickness of the adhesive layer (t_a), while Case 3 contributes to the Mode II stress intensity factor (K_{II}). Note that the lap-shear loading conditions considered in Figure 3b assumed that the backing plates were used, as illustrated in Figure 1b. As a result, m_0 can be expressed as $m_0 = f_0(t + t_a)/2$. Then, the fracture mechanics problems associated the coach-peel and lap-shear specimens in Figure 1 are now transformed to three basic fracture mechanics problems, namely, Cases 1 through 3, for the development of closed-form solutions.

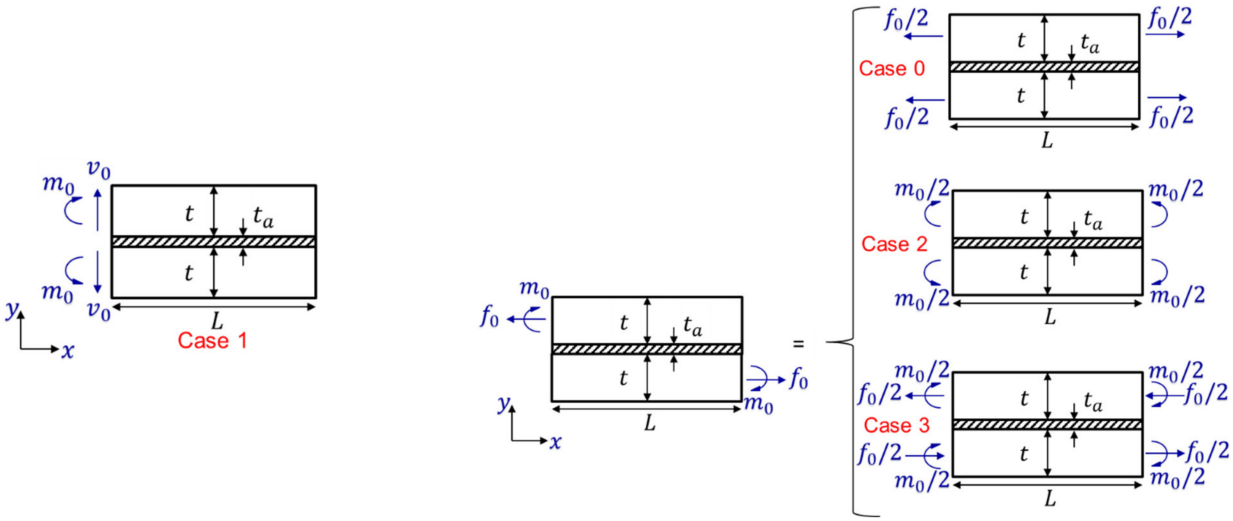

(**a**): Case 1 (**b**): Case 0, 2 and 3

Figure 3. The sandwich model representations of the lap-shear and coach-peel loading conditions through the loading mode deposition. (**a**) Case 1 corresponds to the coach-peel loading condition. (**b**) Cases 0, 2, and 3 correspond to the decompositions of lap-shear loading condition.

2.2. Closed-Form Stress Intensity Factor Solutions

2.2.1. Case 1

Consider a sandwich specimen containing a symmetrically positioned crack of a and remaining ligament of L, as shown in Figure 4a. Its Mode I stress intensity factor (SIF) can be derived by defining a corresponding elastic foundation problem, as shown in Figure 4b. It should be pointed out that Figure 4b looks rather similar to the elastic foundation problem introduced by Kanninen [41] as a double cantilever beam for deriving the K_I expression corresponding to the symmetrically positioned crack in a homogenous specimen (i.e., $t_a = 0$ in Figure 4a). In this study, the adhesive layer t_a was considered here by defining a composite spring representation of the elastic foundation with a spring length $(t + t_a)/2$. The resulting composite spring (two in series) constant can be expressed as follows, as given in Appendix A in detail:

$$k_c = \frac{2EE_a}{Et_a + E_a t} \tag{1}$$

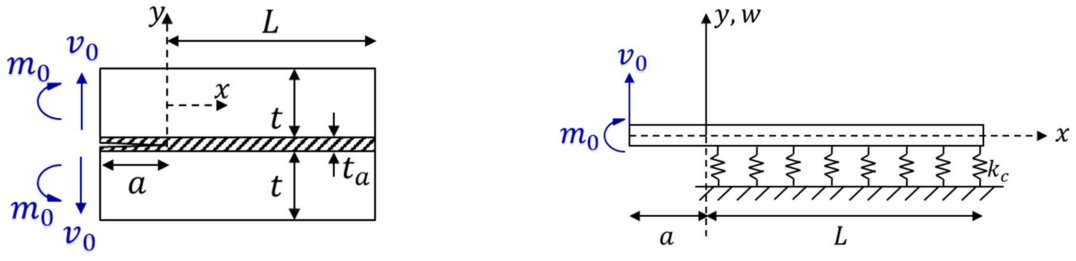

(**a**) (**b**)

Figure 4. The crack problem definition for Case 1. (**a**) Geometry and load conditions. (**b**) Elastic foundation idealization.

By taking advantage of the double cantilever beam solution given by Kanninen [41], the governing equation for the beam situated on the elastic foundation with spring constant k_c can be written as:

$$E\,I\,\frac{d^4w}{dx^4} = \begin{cases} -k_c w(x), & when\ x > 0 \\ 0, & when\ x \le 0 \end{cases} \tag{2}$$

where E is the Young's modulus; I is the moment of inertia; k_c is the spring constant; and $w(x)$ is the deflection of the beam neutral axis. The resulting K_I can be derived in two parts. One is due to the contribution by the transverse force v_0:

$$K_I^{v_0} = 2\sqrt{3}\frac{v_0}{\beta t^{3/2}}\left[\beta a\left(\frac{sinh^2(\beta L)+sin^2(\beta L)}{sinh^2(\beta L)-sin^2(\beta L)}\right)+\left(\frac{sinh(\beta L)cosh(\beta L)-sin(\beta L)cos(\beta L)}{sinh^2(\beta L)-sin^2(\beta L)}\right)\right] \quad (3)$$

which corresponds to the imposition of the following boundary conditions in solving Equation (2):

$$w''(-a) = 0,\ EIw'''(-a) = v_0,\ and\ w''(L) = w'''(L) = 0 \quad (4)$$

The other part is due to the contribution by moment m_0, as:

$$K_I^{m_0} = 2\sqrt{3}\frac{m_0}{t^{3/2}}\left(\frac{sinh^2(\beta L)+sin^2(\beta L)}{sinh^2(\beta L)-sin^2(\beta L)}\right) \quad (5)$$

which corresponds to the imposition of the following boundary conditions in solving Equation (2):

$$EIw''(-a) = m_0,\ w'''(-a) = 0,\ and\ w''(L) = w'''(L) = 0 \quad (6)$$

In Equations (3) and (5), β can be expressed as:

$$\beta = \left(\frac{k_c}{4EI}\right)^{1/4} = \left(\frac{6E_a t}{Et_a + E_a t}\right)^{1/4}\frac{1}{t} \quad (7)$$

The detailed derivations can be found in Appendix A.

2.2.2. Case 2

The fracture mechanics problem corresponding to Case 2 (see Figure 3b) is described in Figure 5a. Its elastic foundation idealization is similar to the one in Figure 4b, but subjected to m_0 and the symmetry conditions as shown in Figure 5b. The corresponding governing equation can be written in a similar manner to the one shown in Equation (2) as:

$$E\,I\,\frac{d^4w}{dx^4} = \begin{cases} -k_c w(x), & \text{when } 0 < x < L \\ 0, & \text{when } x \le 0 \end{cases} \quad (8)$$

with the following boundary conditions:

$$EIw''(-a) = m_0,\ w'''(-a) = 0 \ \text{ and } w'(L) = w'''(L) = 0 \quad (9)$$

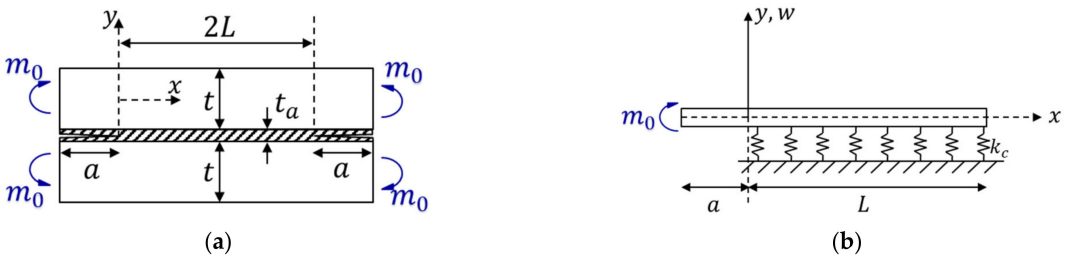

Figure 5. The crack problem definition for Case 2. (**a**) Geometry and load conditions. (**b**) Elastic foundation idealization.

By following the similar derivation process that leads to Equations (3) and (5), it can be seen that the Mode I stress intensity factor corresponding to Case 2 can be expressed as:

$$K_I = 2\sqrt{3}\frac{m_0}{t^{3/2}}\left(\frac{sinh(\beta L)cosh(\beta L)-sin(\beta L)cos(\beta L)}{sinh(\beta L)cosh(\beta L)+sin(\beta L)cos(\beta L)}\right) \quad (10)$$

2.2.3. Case 3

Case 3, which is given in Figure 3b, represents the pure Mode II conditions, or anti-symmetric loading with respect to both the crack plane and one-half ligament (i.e., L), as shown in Figure 6a. The corresponding elastic foundation idealization with respect to the composite shear springs is given in Figure 6b. As such, the loads are anti-symmetric along both coordinate axes. The composite shear spring constant can be shown to have the following expression (see Appendix A):

$$k_s = \frac{2GG_a(t+t_a)}{Gt_a + G_a t} \tag{11}$$

where G and G_a are the shear modulus of the adherend and adhesive, respectively. An average shear strain in the x direction can be defined as:

$$\varepsilon_{xy}(x) = \frac{1}{2}(w'(x) + \frac{2u(x)}{t}) \tag{12}$$

where w and u are the beam deflection and axial displacement in x, respectively. The governing equations become:

$$\begin{aligned} EIw'''(x) &= \tfrac{tk_s}{4}\left(w'(x) + \tfrac{2u(x)}{t}\right) \\ u''(x) &= \tfrac{\tau(x)}{Et} = \tfrac{k_s}{2Et}\left(w'(x) + \tfrac{2u(x)}{t}\right) \end{aligned} \tag{13}$$

The corresponding boundary conditions are:

$$m(0) = m_0,\ f(0) = f_0,\ w''(L) = 0,\ w(L) = 0,\ f(L) = 0, \text{ and } w'(L) = \frac{2u(L)}{t} \tag{14}$$

By following a similar process used in Cases 1 and 2, the resulting Mode II stress intensity factor K_{II} can be expressed as (see Appendix B for details):

$$K_{II} = \frac{2f_0}{\sqrt{t}} coth(\lambda L) \text{ where } \lambda = \sqrt{\frac{4k_s}{Et^2}} = \frac{2}{t\sqrt{1+v}}\sqrt{\frac{G_a(t+t_a)}{Gt_a + G_a t}} \tag{15}$$

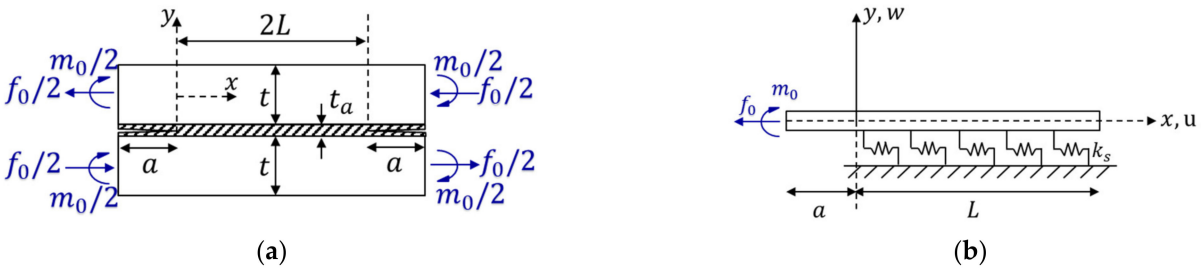

Figure 6. The crack problem definition for Case 3. (**a**) Geometry and load conditions. (**b**) Elastic foundation idealization.

2.3. Analytical Results and Implications

To gain insights into the closed-form solutions developed in Section 2.2 above, the non-dimensional plots of the stress intensity factors with selected geometry and loading conditions of interest to later discussions are plotted in Figure 7. The x-axis is the bond length divided by the substrate thickness L/t. The y-axis is the stress intensity factor divided by the corresponding load and exponents of thickness $\frac{K}{\frac{m_0}{t\sqrt{t}}}$, $\frac{K}{\frac{v_0}{\sqrt{t}}}$, *or* $\frac{K}{\frac{f_0}{\sqrt{t}}}$. Note that the symbols represent the finite element computation results for validation purposes, which will be discussed in the next section (Section 2.4). The following observations can be made:

conditions of interest to later discussions are plotted in Figure 7. The x-axis is the bond length divided by the substrate thickness L/t. The y-axis is the stress intensity factor divided by the corresponding load and exponents of thickness $\frac{K}{\frac{m_0}{t\sqrt{t}}}, \frac{K}{\frac{v_0}{\sqrt{t}}}, or\ \frac{K}{\frac{f_0}{\sqrt{t}}}$. Note that the symbols represent the finite element computation results for validation purposes, which will be discussed in the next section (Section 2.4). The following observations can be made:

1. In all cases, when L/t was large enough (e.g., L/t >3), the SIF values approached a constant value, or their magnitudes (see Figure 7a,c,d) or a constant slope (see Figure 7b). These results suggest that there exists a threshold or critical L/t value (beyond which an increase in bond length does not significantly increase the SIFs).
2. When the L/t was smaller than about 3, the SIFs in Cases 1 (Figure 7a,b) and 3 (Figure 7d) increased rapidly, indicating that in this regime, the bond length was too small to ensure an adequate load-carrying capacity of the joint. The only exception to the above observations was that Case 2 exhibited a decrease in the SIF as L/t approached 0. This trend makes sense, as shown in Figure 5, in that under symmetric moment loading, the crack opening action rapidly diminished as L/t approached zero.
3. When the adhesive layer (t_a) was considered, the non-dimensional variable $E_a t/E t_a$, t/t_a, and G/G_a showed a noticeable influence on the non-dimensional SIFs. When the adhesive layer was thin (i.e., t_a/t small) or stiff (i.e., E_a/E large), the SIF results approached those without considering an adhesive layer (i.e., $t_a = 0$) and vice versa.

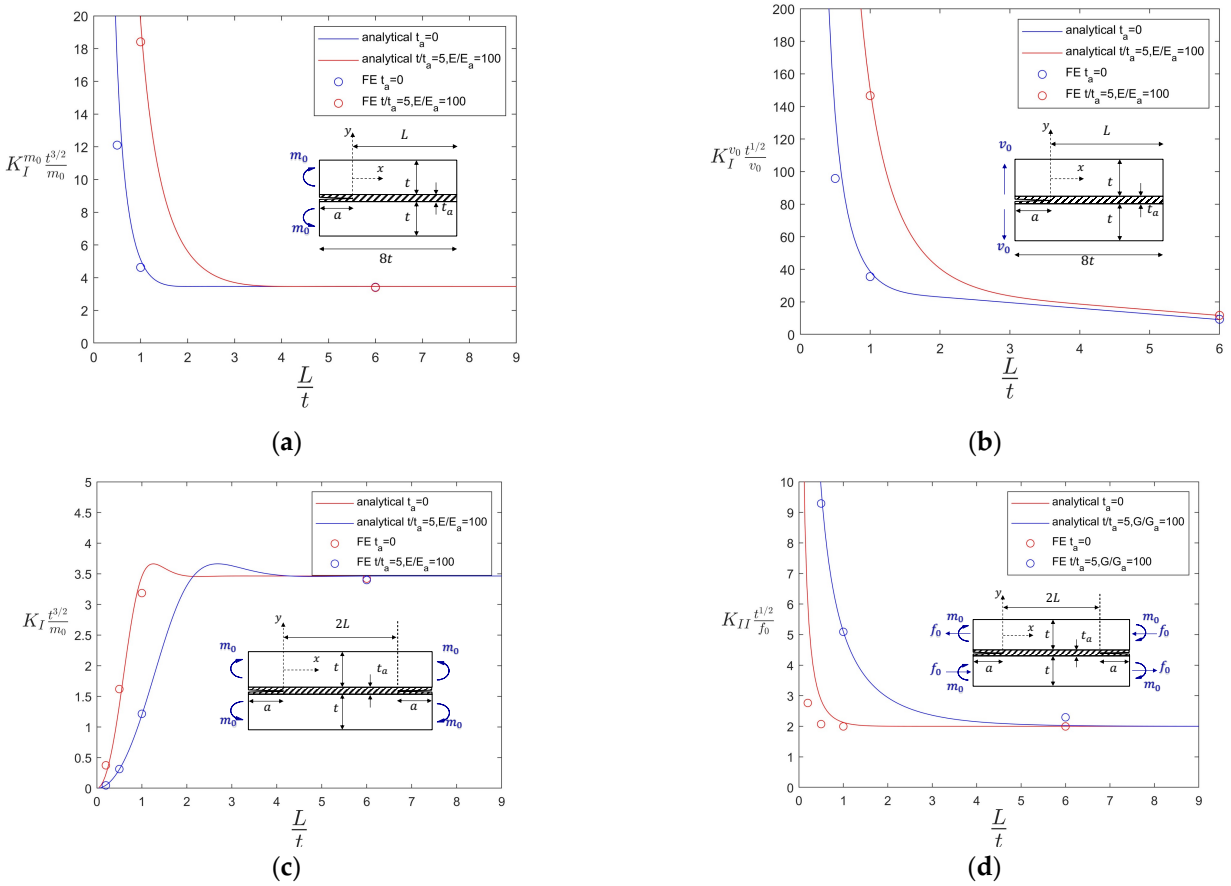

Figure 7. The normalized stress intensity factor as a function of L/t: analytical versus FE validation results. (**a**) Case 1 with moment m_0 on one side. (**b**) Case 1 with transverse load v_0 on one side. (**c**) Case 2 with moment m_0 on two sides. (**d**) Case 3 with both moment m_0 and tension force f_0 on two sides.

2.4. FE Validations

Finite element models were used to validate the analytical solutions developed in the above section. For this purpose, a well-established crack closure integral method [42,43] was adopted here. As illustrated in Figure 8, the method followed a two-step procedure. The first step was to perform finite element computation to obtain nodal forces with respect to a crack body with an initial crack size a_0 (indicated by dashed lines in Figure 8a). The second is to advance the initial crack by Δa corresponding to one element size on the crack

plane and obtain the nodal displacements (see solid lines in Figure 8a). The crack advance increment Δa needs to be small enough to be accurate, as demonstrated for Mode I and the mixed mode crack problems in [42]. The resulting energy release rate can be expressed as the work required to close the crack. Under linear elastic deformation conditions, the work equals one-half of the nodal force before the crack advances Δa by the corresponding displacement difference after the crack advances by Δa, which can be expressed as:

$$\begin{aligned} \mathrm{G_I} &= \lim_{\Delta \mathrm{a} \to 0} \frac{1}{2\Delta \mathrm{a}} F_y(\mathrm{w_1} - \mathrm{w_2}) \\ \mathrm{G_{II}} &= \lim_{\Delta \mathrm{a} \to 0} \frac{1}{2\Delta \mathrm{a}} F_x(\mathrm{u_1} - \mathrm{u_2}) \end{aligned} \tag{16}$$

where F_x and F_y are the nodal forces perpendicular or along the crack growth direction in Step 1; and w and u are the displacements perpendicular or along the crack growth direction of nodes 1 and 2 in Step 2. Then, the SIFs can be obtained as:

$$\begin{aligned} K_I &= \sqrt{G_I E} \\ K_{II} &= \sqrt{G_{II} E} \end{aligned} \tag{17}$$

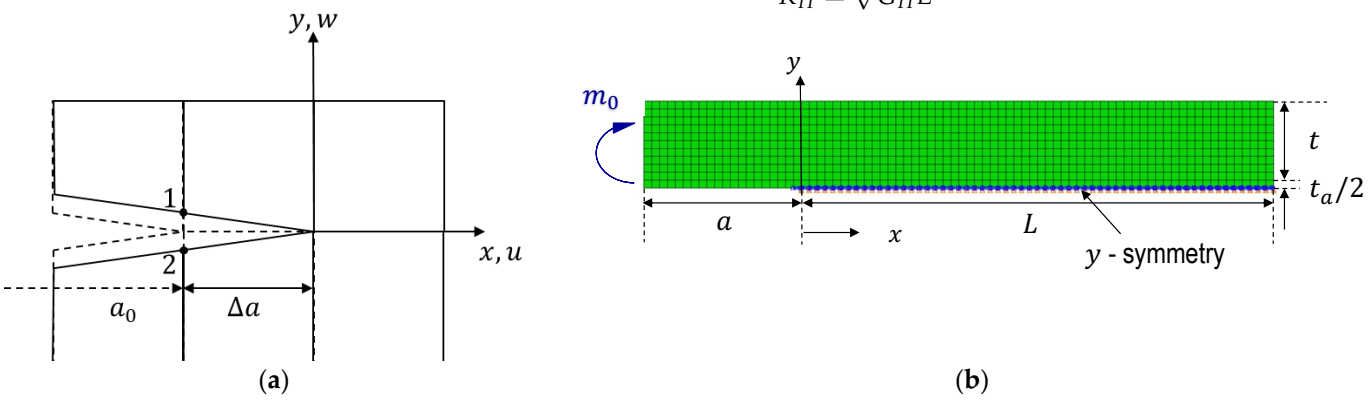

Figure 8. The crack closure integral method and implementation in the SIF calculation in this study. (**a**) Crack closure integral illustration. (**b**) A representative 2D FE model used for Case 1 in Figure 7a.

An effective SIF for the mixed mode crack problem becomes:

$$K_e = \sqrt{{K_I}^2 + {K_{II}}^2} \tag{18}$$

Two-dimensional (2D) plane stress ("CPS4" in ABAQUS) FE models with an element size approximate to 0.5 mm (0.1t) along the x direction was used to provide a sufficient resolution of SIF as a function crack size. As illustrated in Figure 8b, a crack size of a situated within the mid-thickness of the adhesive layer was introduced. Half symmetry conditions (i.e., y symmetry in ABAQUS) were considered, which corresponded to Case 1 in Figure 7a. All FE models used had the same overall dimensions of $L + a = 40$ mm and $t = 5$ mm and dimensionless sandwich properties $t/t_a = 5$, $E/E_\mathrm{a} = 100$, and $v = v_a = 0.3$. In addition, the homogenous condition (i.e., $t_\mathrm{a} = 0$) was also considered for comparison purposes. It should be noted that the case in Figure 7d corresponds to the anti-symmetry with respect to the crack plane (i.e., x anti-symmetry in ABAQUS) and the transverse plane in the middle of the bond line (i.e., y anti-symmetry in ABAQUS). As the crack size a increased, the corresponding nodes were sequentially deactivated along the crack plane. The final SIF results are shown in Figure 7 as symbols. The agreement between the analytical and FE results were evident.

3. Applications in Fatigue Test Data Analysis

3.1. Fatigue Test Details

To demonstrate the applications of the stress intensity factor solutions developed for the adhesive bonded sandwich specimens in Section 2, here, we considered the fatigue tests

conducted by Chen et al. [1]. The adhesive bonded fatigue test specimens used in [1] were of two types: lap-shear and coach-peel. The adherend material was aluminum A5754-O, with a Young's modulus of 68,948 MPa and Poisson's ratio of 0.33. The adhesive material was BETAMATE4601, with a Young's modulus of 2860 MPa and Poisson's ratio of 0.35. The specimen width was 25.4 mm. Other specimen geometry details are shown in Figure 9 [1]. The adhesive thickness was reported to be 0.275 mm, while the two adherend thicknesses (t_1 and t_2) were considered, as summarized in Table 1, as taken from [1].

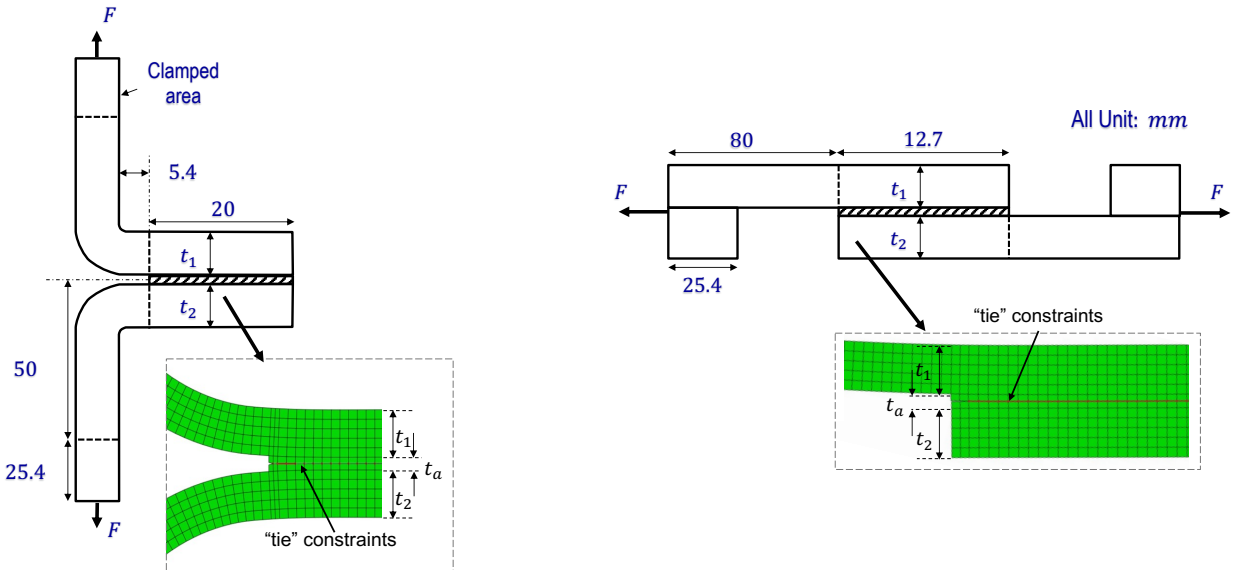

Figure 9. The test specimen geometry and dimensions (unit: mm) [1]. (**a**) Coach-peel; (**b**) Lap-shear.

Table 1. The adherend thickness combinations of the specimens [1].

Joint Types	Adherend Thickness Combinations
Lap-shear t_1–t_2	1 mm–1 mm 1 mm–2 mm 2 mm–2 mm
Coach-peel t_1–t_2	1 mm–1 mm 1 mm–2 mm 2 mm–2 mm

Fatigue tests were conducted with a load ratio R = 0.1 and a frequency of 40 Hz. The failure criterion used was complete joint separation through cohesive failure within the adhesive layer. The run-out criterion was set as 10^7 cycles, which was not considered in this study.

3.2. SIFs for Coach-Peel Test Specimens

For the coach-peel test specimens with $t_1 = t_2 = t$, the SIF solution developed for Case 1 with the transverse load Equation (3), was directly applicable here, by setting $L + a = 25.4\text{ mm} + t_1/2$, corresponding to the dimensions shown in Figure 9a. Note that in these coach-peel specimens, the initial crack size a in Equation (2) represents the distance between the position load projected to the crack plane and the position where the adhesive layer starts (c in Figure 1a). The non-dimensional analytical results of 1 mm–1 mm are shown in Figure 10 along with the FE results as a validation. The x- and y-axis definitions are the same as Figure 7b. For $t_1 \neq t_2$, the FE solutions based on the crack closure integral described in Figure 8 were used here. See the FE model for simulating the coach-peel loading conditions shown as the insert in Figure 9a.

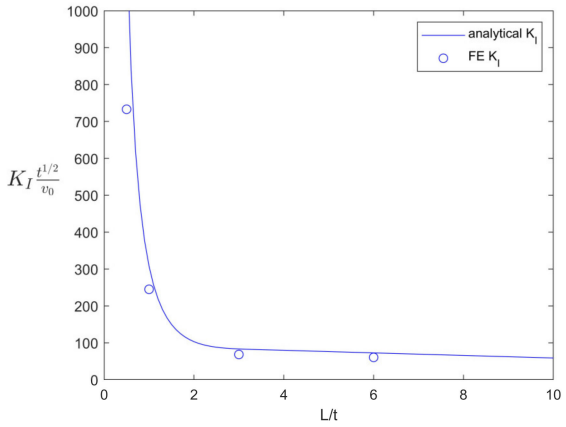

Figure 10. The SIF results: the analytical versus the FE results for the coach-peel test specimens.

3.3. SIFs for Lap-Shear Test Specimens

For analyzing the lap-shear test specimens, Case 2 and Case 3 contributed to K_I (through Equation (10)) and K_{II} (through Equation (15)), respectively. The combined effective SIF can be obtained from Equation (18), leading to:

$$K_e = \frac{f_0}{\sqrt{t}}\sqrt{\frac{3}{4}\left(\frac{t+t_a}{t}\right)^2\left(\frac{sinh(\beta L)\,cosh(\beta L)-sin(\beta L)\,cos(\beta L)}{sinh(\beta L)\,cosh(\beta L)+sin(\beta L)\,cos(\beta L)}\right)^2+[\coth(\lambda L)]^2} \quad (19)$$

Both the analytical and FE non-dimensional results were compared in Figure 11, corresponding to $t_1 = t_2 = 1$ mm. The x- and y-axis definitions are the same as Figure 7d. Note that the total bond length was $2(L + a) = 12.7$ mm, corresponding to the lap-shear specimen shown in Figure 9b. Again, for $t_1 \neq t_2$, the FE results based on the crack closure integral method shown in Figure 8 were used to correlate the fatigue test data in this study. See the FE model to simulate the lap-shear loading conditions shown as the insert in Figure 9b.

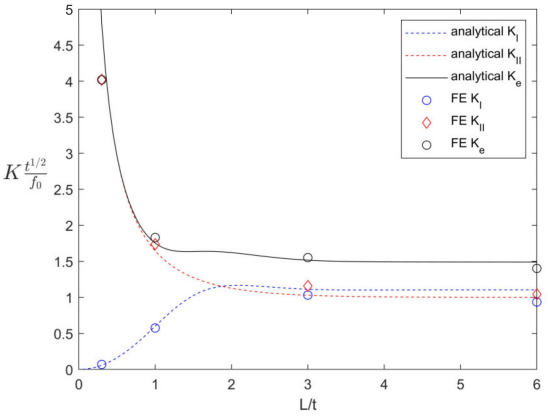

Figure 11. The SIF results: the analytical versus FE solutions for the lap-shear test specimen.

3.4. Fatigue Test Data Correlation Using SIFs

It is important to note that the SIF value results shown in Figures 10 and 11 become essentially stabilized as long as the initial bond length L/t is larger than 2. As such, the combined stress intensity factor range ΔK_e, given in Equations (3) and (19), can be used to describe the fatigue crack propagation behaviors of the test specimens described in Section 3.1. For comparison purposes, the effective SIF corresponding to the applied line force (N/mm) of unity, designated as K_e^u $(MPa\sqrt{m})$, for the two specimen types shown in Figure 9 and different thickness combinations are shown in Figure 12.

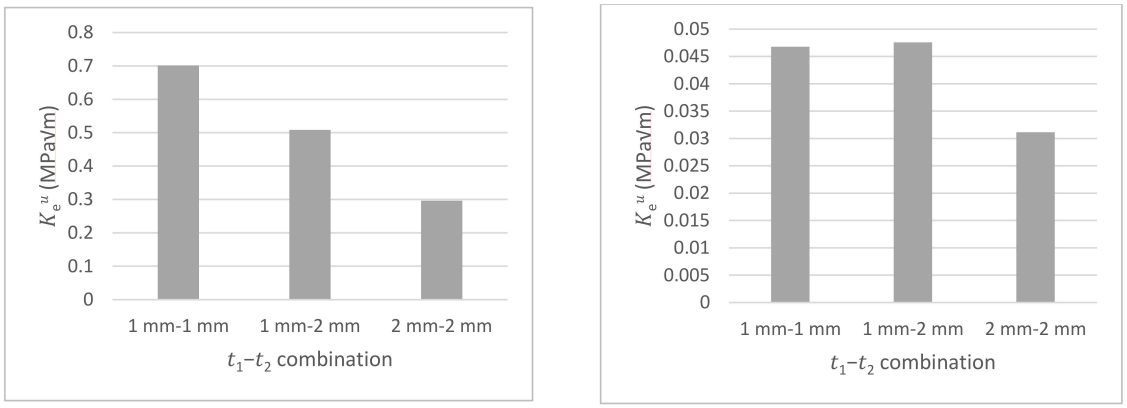

(**a**) (**b**)

Figure 12. The comparison of SIF values over different specimen types and thickness combinations. (**a**) Coach–peel. (**b**) Lap–shear.

The cohesive failure fatigue test data from [1] is presented in Figure 13a as a nominal stress range ($\Delta\sigma_n$) versus the cycles to failure in the log–log scale. Here, the nominal stress range is defined as the remote load range ΔF divided by the adhesive bond area (i.e., $A = L_o \times W$, in which L_o is the bond length). Not surprisingly, the test data exhibited significant scatter, as shown in Figure 13a, particularly between the coach-peel and lap-shear specimen types. With the SIF values given in Figure 12, corresponding to the unit line force, the nominal stress range in Figure 13a can be converted to the equivalent stress intensity factor range (ΔK_e) through:

$$\Delta K_e = \Delta\sigma_n \times L_o \times K_e^u \tag{20}$$

where $\Delta\sigma_n$ is the nominal stress range and K_e^u is the effective SIF under unit line force. Figure 13b shows the same fatigue test data in terms of ΔK_e versus the cycles to failure. It is evident that ΔK_e is effective in correlating the same test data shown in Figure 13a in which differences between the coach-peel and lap-shear specimens are no longer obvious. To further delineate the data trend, all coach-peel test data were further evaluated by comparing the nominal stress range with the equivalent stress intensity factor range, as shown in Figure 14. The results in Figure 14 further illustrate the ability of ΔK_e in reconciling the differences in the fatigue data that resulted from the different thickness combinations in the test specimens.

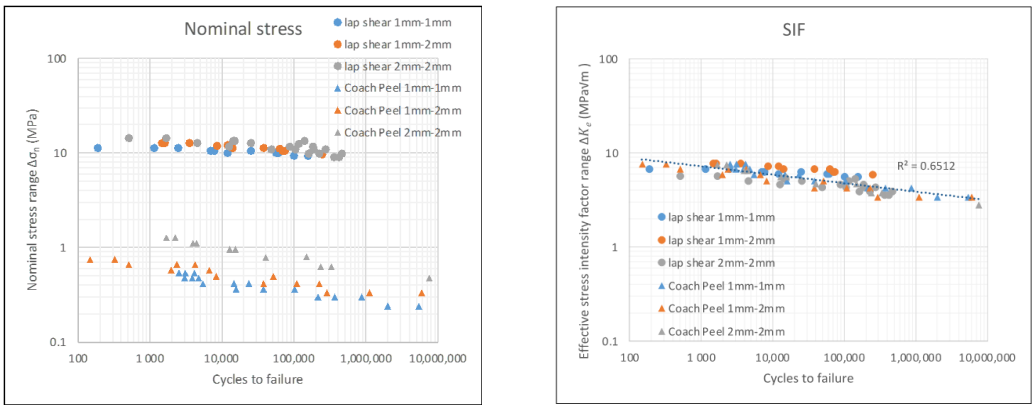

(**a**) (**b**)

Figure 13. The test data correlation for both the coach-peel and lap-shear specimens. (**a**) Nominal stress range. (**b**) Effective stress intensity factor range.

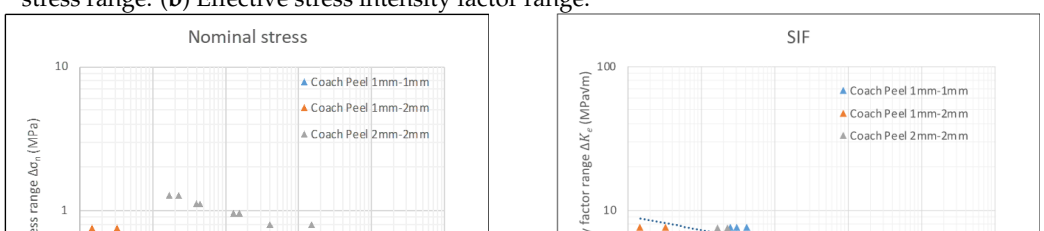

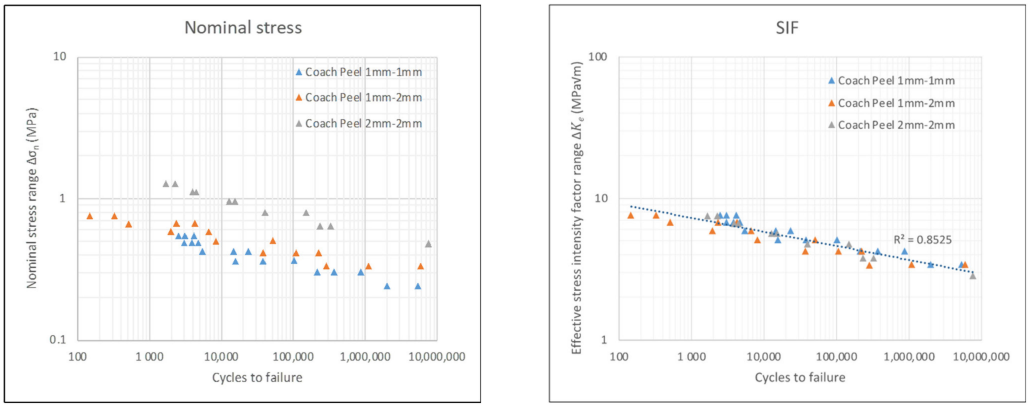

(**a**) (**b**)

Figure 14. The test data correlation of the coach-peel test specimens. (**a**) Nominal stress range. (**b**) Effective stress intensity factor range.

4. Discussions

4.1. Existence of Critical Bond Length

As discussed in Section 2.3, there exists a threshold or critical bond length (L_c/t) in terms of L/t beyond which the SIF values tend to become stabilized. This can have important engineering implications in the optimum joint design to ensure that the adhesive bond length L is somewhat larger than L_c, but not too large to incur manufacturing costs and adding weight. For illustration purposes, we can define the critical bond length L_c as the length within which $K \geq 1.05K_0$. Here, K_0 represents the stabilized value corresponding to the infinitely long bond line. Figures 15 and 16 show the results corresponding to Case 1 (see Section 2.2.1) subjected to the pure moment m_0 loading. In Figures 15a and 16a, the x- and y-axis definitions were the same as in Figure 7a. Figures 15b and 16b demonstrate how the non-dimensional critical bond length L_c/t is influenced by the non-dimensional thickness ratio t/t_a or non-dimensional Young's modulus ratio E/E_a. The reference solution corresponds to the sandwich geometry and property combinations associated with the test specimens used in [1], as summarized in Section 3.1. As shown in Figure 15, as t/t_a increases, the non-dimensional critical length (L_c/t) decreases, approaching the value corresponding to $t/t_a \to \infty$ (i.e., a homogenous specimen condition without the presence of an adhesive layer). For the given reference thickness ratio of $t/t_a = 3.63$, consistent with the test data (see Section 3.1), the dependency of the critical bond length L_c/t on the Young's modulus ratio (E/E_a) is shown in Figure 16. As E/E_a reaches about 250, the non-dimensional critical bond length approximately reaches a stabilized value of about 2.5.

Metals **2022**, *12*, x FOR PEER REVIEW 14 of 21

Figure 15, as t/t_a increases, the non-dimensional critical length (L_c/t) decreases, approaching the value corresponding to $t/t_a \to \infty$ (i.e., a homogenous specimen condition without the presence of an adhesive layer). For the given reference thickness ratio of $t/t_a = 3.63$, consistent with the test data (see Section 3.1), the dependency of the critical bond length L_c/t on the Young's modulus ratio (E/E_a) is shown in Figure 16. As E/E_a reaches about 250, the non-dimensional critical bond length approximately reaches a stabilized value of about 2.5.

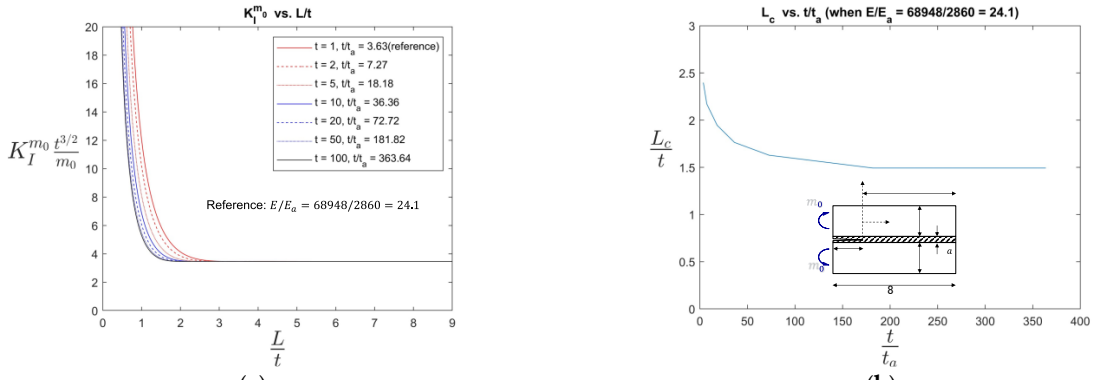

(**a**) (**b**)

Figure 15. Normalized critical bond length L_c/t as a function of t/t_a—Case 1 subjected to pure moment m_0 with $\frac{E}{E_a} = 24.1$. (**a**) Normalized K_I as a function of L/t. (**b**) Normalized critical bond length (L_c/t) as a function of t/t_a.

(**a**) (**b**)

Figure 15. Normalized critical bond length L_c/t as a function of t/t_a—Case 1 subjected to pure moment m_0 with $\frac{E}{E_a} = 24.1$. (**a**) Normalized K_I as a function of L/t. (**b**) Normalized critical bond length (L_c/t) as a function of t/t_a.

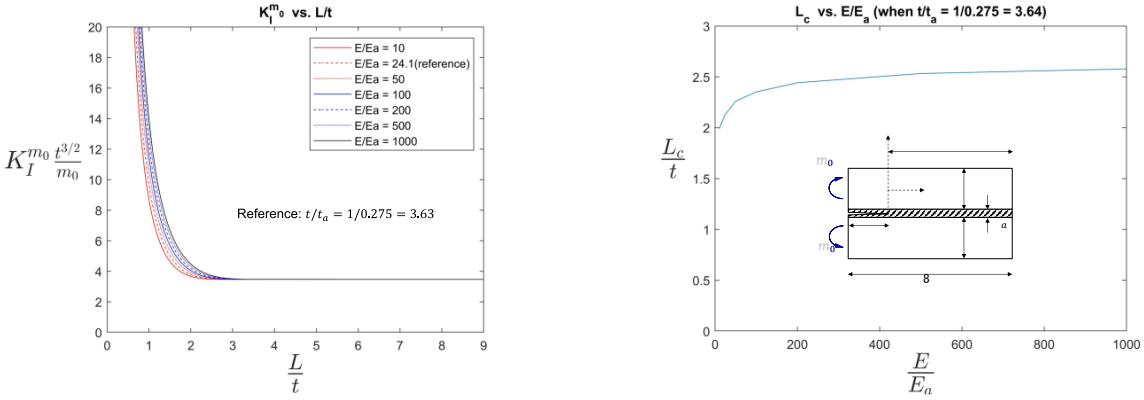

(**a**) (**b**)

Figure 16. The normalized critical bond length L_c/t as a function of E/E_a—Case 1 subjected to the pure moment m_0 with $t/t_a = 3.63$. (**a**) Normalized K_I as a function of L/t. (**b**) Normalized critical bond length (L_c/t) as a function of E/E_a.

4.2. ΔK_e as a Fatigue Parameter

For adhesive-bonded metal to metal joints, decohesion fatigue failure confined within the adhesive layer seems common in the fatigue test data reported in the literature as reviewed as a part of this study. This was definitely the case for the test data studied in this paper, as documented in Section 3.1 for the coach-peel and lap-shear specimens. As long as $L/t > L_c/t$, the resulting SIFs had an approximately constant value regardless of the crack size (see Figures 14 and 15). As such, ΔK_e can be argued to serve as an appropriate fatigue parameter, as demonstrated in Figures 13 and 14.

It is worth noting that for structural applications, the closed-form stress intensity factor solutions needed for computing ΔK_e can be implemented by obtaining the line forces f_0, v_0 and line moment m_0, described in Figure 3 through nodal forces and nodal moments available in the structural FE results by using the simultaneous equation method presented in [44–46]. As such, complex 3D adhesive joint stress calculation problems can be transformed into an equivalent 2D sandwich specimen problem. Such 3D implementations for structural applications will be discussed in a future publication.

It should also be pointed out that the present analytical solutions are limited to $t_1 = t_2 = t$. For sandwich specimens with unequal thickness combinations, further developments on the approximate stress intensity factor solutions are needed to extend the generality of the present approach, which will be reported in the near future.

5. Conclusions

In this paper, a set of closed-form stress intensity factor solutions for a general sandwich specimen containing an adhesive layer was presented by considering the traction loading conditions involved in commonly used lap-shear and coach-peel test specimens. The analytical solutions based on a novel elastic foundation idealization were validated through direct finite element computations. The results show that the resulting equivalent stress intensity factor ΔK_e is effective in correlating the fatigue test data from the adhesive joints. In addition, the analytical solutions show that there exists a threshold bond layer length (L_c/t) beyond which the stress intensity factor value become stabilized, which can be used to determine the minimum bond area for achieving the optimum joint design in practice. The stress intensity factor solutions are transferable to a general 3D structural environment through the determination of the relevant line forces and moment shown in Figure 3 by an existing traction-based structural stress method already in the literature.

Author Contributions: Problem definition and technical approach, P.D.; Analytical derivations and validations, Y.Z. and X.P.; Detailed case studies and drafting manuscript, Y.Z.; Resources, manuscript review, and editing, P.D. All authors have read and agreed to the published version of the manuscript.

Funding: The first two authors (Y.Z. and P.D.) were funded by the National Science Foundation (NSF Grant No. CMMI 2126163).

Institutional Review Board Statement: Not applicable.

Informed Consent Statement: Not applicable.

Data Availability Statement: Not applicable.

Acknowledgments: The first two authors (Y.Z. and P.D.) acknowledge the support of the National Science Foundation grant (NSF Grant No. CMMI 2126163) at the University of Michigan.

Conflicts of Interest: The authors declare no conflict of interest.

Appendix A. Derivation of Composite Spring Constant

Appendix A.1. Spring Constants Corresponding to Cases 1 and 2

First, we can consider the spring constant of the isotropic beam (i.e., $t_a = 0$). Assume that each segment of a beam (unit length and unit width) is a bar under tension force F, as shown in Figure A1a, then the average strain is:

$$\varepsilon = \frac{\sigma}{E} = \frac{\frac{F}{A}}{E} = \frac{F}{E} \tag{A1}$$

Then, the deflection at the neutral axis is:

$$w = \varepsilon \times \frac{t}{2} = \frac{Ft}{2E} \tag{A2}$$

Then, the spring constant can be obtained:

$$k_c = \frac{F}{w} = \frac{2E}{t} \tag{A3}$$

The corresponding β is:

$$\beta = \left(\frac{k_c}{4EI}\right)^{\frac{1}{4}} = \frac{6^{1/4}}{t} \tag{A4}$$

Now, if the beam is a composite beam, we have bar 1 with t_1, E_1 and bar 2 with t_2, E_2. Assuming that we know the displacement at the neutral axis of bar 1 is w_{eq}, as shown in Figure A1b, we can find the strain of each beam:

$$\varepsilon_1 = \frac{\sigma}{E_1} = \frac{F/A}{E_1} = \frac{F}{E_1};\ \varepsilon_2 = \frac{F}{E_2} \tag{A5}$$

Then, the equivalent deflection can be:

$$w_{eq} = \varepsilon_1 \times \frac{t_1}{2} + \varepsilon_2 \times t_2 \tag{A6}$$

And the equivalent spring constant is:

$$k_{ceq} = \frac{F}{w_{eq}} = \frac{F}{\frac{Ft_1}{2E_1} + \frac{Ft_2}{E_2}} = \frac{2E_1E_2}{2E_1t_2 + E_2t_1} \tag{A7}$$

In a sandwich model with $t_1 = t$, $E_1 = E$, $t_2 = t_a/2$, and $E_2 = E_a$, the constant is:

$$k_{ceq} = \frac{2EE_a}{Et_a + E_at} \tag{A8}$$

The corresponding β is:

$$\beta = \left(\frac{k_{ceq}}{4EI}\right)^{1/4} = \left(\frac{6E_a t}{Et_a + E_a t}\right)^{1/4} \frac{1}{t} \tag{A9}$$

Note that when dealing with composite beams, it is assumed that the area outside the bond area is one beam with E and t. This is more like an adhesive failure (i.e., the crack propagates at the interface between adhesive and adherend). However, when the adhesive is thin and negligible, this can be used in cohesive failure, whose crack goes through the adhesive layer.

Figure A1. A diagram of determining the spring constant. (**a**) Isotropic beam. (**b**) Composite beam.

Appendix A.2. Composite Shear Spring Constant Corresponding to Case 3

Similar to Appendix A1, we can consider the shear spring constant of the isotropic beam, (i.e., $t_a = 0$.) According to the stress–strain relationship,

$$\tau = k_s \varepsilon_{xy} = 2G\varepsilon_{xy} \tag{A10}$$

It is easy to find:

$$k_s = 2G = \frac{E}{1+v} \tag{A11}$$

And the corresponding λ is:

$$\lambda = \sqrt{\frac{4k_s}{Et^2}} = \frac{2}{t\sqrt{1+v}} \tag{A12}$$

In a composite beam with t_1, E_1 and t_2, E_2, as shown in Figure A2, the equivalent axial displacement is u_{eq}. Since the shear strain is related to the displacement of both directions, it is hard to find the equivalent displacement unless we assume $w = 0$ and consider u only. Therefore, we can define the strain–displacement relationship as:

$$\varepsilon_{xy} = \frac{1}{2}\left(\frac{2u}{t}\right) = \frac{u}{t},\ u = 2\varepsilon_{xy} * \frac{t}{2} \tag{A13}$$

We can find the strain of each beam:

$$\varepsilon_{xy1} = \frac{T}{2G_1},\ \varepsilon_{xy2} = \frac{T}{2G_2} \tag{A14}$$

Then, the equivalent axial displacement can be:

$$u_{eq} = 2(\varepsilon_{xy1} \times \frac{t_1}{2} + \varepsilon_{xy2} \times t_2) \tag{A15}$$

And the equivalent strain is:

$$\varepsilon_{xyeq} = \frac{1}{2}\frac{u_{eq}}{t_{eq}} = \frac{\varepsilon_{xy1} \times \frac{t_1}{2} + \varepsilon_{xy2} \times t_2}{\frac{t_1}{2} + t_2} \tag{A16}$$

The equivalent spring constant is:

$$k_{seq} = \frac{T}{\varepsilon_{xyeq}} = \frac{2G_1G_2(t_1 + 2t_2)}{2G_1t_2 + G_2t_1} \tag{A17}$$

In a sandwich model with $t_1 = t$, $G_1 = G$, $t_2 = t_a/2$, and $G_2 = G_a$, the constant is:

$$k_{seq} = \frac{2GG_a(t + t_a)}{Gt_a + G_at} \tag{A18}$$

The corresponding λ is:

$$\lambda = \sqrt{\frac{4k_{seq}}{Et^2}} = \frac{2}{t\sqrt{1+v}}\sqrt{\frac{G_a(t + t_a)}{Gt_a + G_at}} \tag{A19}$$

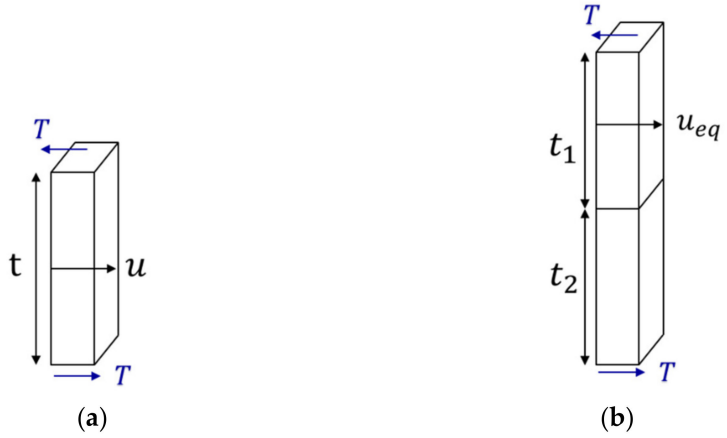

Figure A2. A diagram of determining the shear spring constant. (**a**) Isotropic beam; (**b**) Composite beam.

Appendix B. Elastic Foundation Solution with Shear Spring

First, we can consider an isotropic beam (i.e., $t_a = 0$). Assume that the shear stress is proportional to the average strain:

$$\tau(x) = k_s\varepsilon_{xy}(x) = \frac{k_s}{2}\left(w'(x) + \frac{2u(x)}{t}\right) \tag{A20}$$

The small segment and loads are shown in Figure A3. The beam bending equation can obtain:

$$EIw''(x) = m(x) \tag{A21}$$

And the moment equilibrium of the small segment is:

$$m'(x) = \tau(x) \times \frac{t}{2} \tag{A22}$$

Therefore, using the derivative of Equation (A21) and combining Equations (A20) and (A22), we can obtain the deflection governing equation:

$$EIw'''(x) = \frac{tk_s}{4}\left(w'(x) + \frac{2u(x)}{t}\right) \tag{A23}$$

However, this equation has $u(x)$ and cannot be solved directly. The stress–strain–displacement relationship in the axial direction is:

$$\frac{du}{dx} = \varepsilon_x = \frac{f(x)}{Et} \tag{A24}$$

And the force equilibrium can be:

$$f'(x) = \tau(x) \tag{A25}$$

Similarly, using the derivative of Equation (A24) and combining Equations (A20) and (A25), we can obtain the axial displacement governing equation:

$$u''(x) = \frac{\tau(x)}{Et} = \frac{k_s}{2Et}\left(w'(x) + \frac{2u(x)}{t}\right) \tag{A26}$$

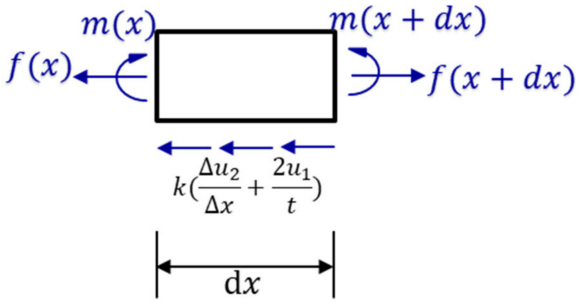

Figure A3. A free body diagram of a small segment of the upper substrate.

Equations (A23) and (A26) are the governing equations of this model. In Case 3, the boundary conditions are:

$$m(0) = m_0 = \frac{f_0 t}{2},\ f(0) = f_0,\ w''(L) = 0,\ w(L) = 0,\ f(L) = 0,\ and\ w'(L) = \frac{2u(L)}{t} \tag{A27}$$

Solving the governing equations, we can obtain the deflection and axial displacement as:

$$\begin{gathered} u(x) = \frac{c_0}{\lambda^2}e^{\lambda x} + \frac{c_1}{\lambda^2}e^{-\lambda x} + c_2 x + c_3 \\ w(x) = \frac{6c_0}{t\lambda^3}e^{\lambda x} - \frac{6c_1}{t\lambda^3}e^{-\lambda x} + c_4 x^2 + c_5 x + c_6 \\ \text{Where } c_0 = -\frac{f_0\lambda}{Et}\frac{e^{-\lambda L}}{e^{\lambda L} - e^{-\lambda L}}, c_1 = -\frac{f_0\lambda}{Et}\frac{e^{\lambda L}}{e^{\lambda L} - e^{-\lambda L}}, c_2 = c_4 = 0, \\ c_3 = -\frac{2f_0}{Et\lambda\left(e^{\lambda L} - e^{-\lambda L}\right)}, c_5 = \frac{4f_0}{Et^2\lambda\left(e^{\lambda L} - e^{-\lambda L}\right)}, c_6 = -\frac{4f_0 L}{Et^2\lambda\left(e^{\lambda L} - e^{-\lambda L}\right)}, \lambda = \sqrt{\frac{4k_s}{Et^2}} \end{gathered} \tag{A28}$$

At the position that load was applied, the rotation angle and axial displacement are:

$$\begin{aligned} w'(-a) &= w'(0) - \frac{12m_0}{Et^3} = -\frac{f_0}{Et^2}\left[\frac{6e^{\lambda L} + 6e^{-\lambda L} - 4}{\lambda\left(e^{\lambda L} - e^{-\lambda L}\right)} + 6a\right] \\ u(-a) &= u(0) - \frac{f_0 a}{Et} = -\frac{f_0}{Et}\left(\frac{e^{\lambda L} + e^{-\lambda L} + 2}{\lambda\left(e^{\lambda L} - e^{-\lambda L}\right)} + a\right) \end{aligned} \tag{A29}$$

The strain energy of each crack is:

$$\Omega = -m_0 \times w'(-a) - f_0 \times u(-a) = \frac{4f_0}{Et^2}\left[\frac{e^{\lambda L} + e^{-\lambda L}}{\lambda\left(e^{\lambda L} - e^{-\lambda L}\right)} + a\right] \tag{A30}$$

Assume that the cracks grow simultaneously from both sides, then at each side, the energy release rate is:

$$G = \frac{\partial \Omega}{\partial a} - \frac{\partial \Omega}{\partial L} = \frac{4f_0}{Et^2}\left(\frac{e^{\lambda L} + e^{-\lambda L}}{e^{\lambda L} - e^{-\lambda L}}\right)^2 \tag{A31}$$

Finally, we can obtain the stress intensity factor:

$$K_{II} = \sqrt{GE} = \frac{2f_0}{\sqrt{t}}\frac{e^{\lambda L} - e^{-\lambda L}}{e^{\lambda L} + e^{-\lambda L}} = \frac{2f_0}{\sqrt{t}}\coth(\lambda L) \tag{A32}$$

When dealing with a composite beam, Equation (A32) can be used by replacing the shear spring into an equivalent shear spring, in which the details can be found in Appendix A.

References

1. Chen, Q.; Guo, H.; Avery, K.; Su, X.; Kang, H. Fatigue performance and life estimation of automotive adhesive joints using a fracture mechanics approach. *Eng. Fract. Mech.* **2017**, *172*, 73–89. [CrossRef]
2. Blanco, D.; Rubio, E.M.; Marín, M.M.; Davim, J.P. Advanced materials and multi-materials applied in aeronautical and automotive fields: A systematic review approach. *Procedia CIRP* **2021**, *99*, 196–201. [CrossRef]
3. Lambiase, F.; Scipioni, S.I.; Lee, C.J.; Ko, D.C.; Liu, F. A State-of-the-Art Review on Advanced Joining Processes for Metal-Composite and Metal-Polymer Hybrid Structures. *Materials* **2021**, *14*, 1890. [CrossRef] [PubMed]
4. Liu, F.; Dong, P. Directly and Reliably Welding Plastic to Metal. *Weld. J.* **2022**, *101*, 45.
5. Dong, P. Quantitative weld quality acceptance criteria: An enabler for structural lightweighting and additive manufacturing. *Weld. J.* **2020**, *99*, 39S–51S. [CrossRef]
6. Liu, F.C.; Dong, P.; Lu, W.; Sun, K. On formation of AlOC bonds at aluminum/polyamide joint interface. *Appl. Surf. Sci.* **2019**, *466*, 202–209. [CrossRef]
7. Liu, F.C.; Dong, P.; Pei, X. A high-speed metal-to-polymer direct joining technique and underlying bonding mechanisms. *J. Mater. Process. Technol.* **2020**, *280*, 116610. [CrossRef]
8. Liu, F.C.; Dong, P.; Zhang, J.; Lu, W.; Taub, A.; Sun, K. Alloy amorphization through nanoscale shear localization at Al-Fe interface. *Mater. Today Phys.* **2020**, *15*, 100252. [CrossRef]
9. Liu, F.; Zhang, Y.; Dong, P. Large area friction stir additive manufacturing of intermetallic-free aluminum-steel bimetallic components through interfacial amorphization. *J. Manuf. Process.* **2022**, *73*, 725–735. [CrossRef]
10. Ha, D.W.; Jeon, G.W.; Shin, J.S.; Jeong, C.Y. Mechanical properties of steel-aluminum multi-materials using a structural adhesive. *Mater. Today Commun.* **2020**, *25*, 101552. [CrossRef]
11. Kinloch, A.; Korenberg, C.; Tan, K.T.; Watts, J. The Durability of Structural Adhesive Joints. In Proceedings of the 7th European Adhesion Conference—EURADH 2004, Freiberg, Germany, 1 September 2004.
12. Gledhill, R.A.; Kinloch, A.J.; Shaw, S.J. A Model for Predicting Joint Durability. *J. Adhes.* **2007**, *11*, 3–15. [CrossRef]
13. Volkersen, O. Die Niektraftverteilung in Zugbeanspruchten mit Konstanten Laschenquerschritten. *Luftfahrtforschung* **1938**, *15*, 41–47.
14. Goland, M.; Buffalo, N.Y.; Reissner, E. The Stresses in Cemented Joints. *J. Appl. Mech.* **1944**, *11*, A17–A27. [CrossRef]
15. Anyfantis, K.N.; Tsouvalis, N.G. Loading and fracture response of CFRP-to-steel adhesively bonded joints with thick adherents—Part I: Experiments. *Compos. Struct.* **2013**, *96*, 850–857. [CrossRef]
16. Davies, P.; Sohier, L.; Cognard, J.Y.; Bourmaud, A.; Choqueuse, D.; Rinnert, E.; Créac'hcadec, R. Influence of adhesive bond line thickness on joint strength. *Int. J. Adhes. Adhes.* **2009**, *29*, 724–736. [CrossRef]
17. Marzi, S.; Biel, A.; Stigh, U. On experimental methods to investigate the effect of layer thickness on the fracture behavior of adhesively bonded joints. *Int. J. Adhes. Adhes.* **2011**, *31*, 840–850. [CrossRef]
18. Boutar, Y.; Naïmi, S.; Mezlini, S.; Da Silva, L.F.M.; Hamdaoui, M.; Ben Sik Ali, M. Effect of adhesive thickness and surface roughness on the shear strength of aluminium one-component polyurethane adhesive single-lap joints for automotive applications. *J. Adhes. Sci. Technol.* **2016**, *30*, 1913–1929. [CrossRef]
19. Monteiro, J.; Akhavan-Safar, A.; Carbas, R.; Marques, E.; Goyal, R.; El-Zein, M.; da Silva, L. Influence of mode mixity and loading conditions on the fatigue crack growth behaviour of an epoxy adhesive. *Fatigue Fract. Eng. Mater. Struct.* **2019**, *43*, 308–316. [CrossRef]
20. Wah, T. Stress Distribution in a Bonded Anisotropic Lap Joint. *J. Eng. Mater. Technol.* **1973**, *95*, 174–181. [CrossRef]
21. Pirvics, J. Two dimensional displacement-stress distributions in adhesive bonded composite structures. *J. Adhes.* **1974**, *6*, 207–228. [CrossRef]
22. Crocombe, A.D.; Bigwood, D.A. Development of a full elasto-plastic adhesive joint design analysis. *J. Strain Anal. Eng. Des.* **1992**, *27*, 211–218. [CrossRef]

23. Adams, R.D.; Mallick, V. A method for the stress analysis of lap joints. *J. Adhes.* **1992**, *38*, 199–217. [CrossRef]
24. Yang, C.; Pang, S.S. Stress-Strain Analysis of Single-Lap Composite Joints Under Tension. *J. Eng. Mater. Technol.* **1996**, *118*, 247–255. [CrossRef]
25. Frostig, Y.; Thomsen, O.T.; Mortensen, F. Analysis of Adhesive-Bonded Joints, Square-End, and Spew-Fillet—High-Order Theory Approach. *J. Eng. Mech.* **1999**, *125*, 1298–1307. [CrossRef]
26. Sawa, T.; Liu, J.; Nakano, K.; Tanaka, J. Two-dimensional stress analysis of single-lap adhesive joints of dissimilar adherends subjected to tensile loads. *J. Adhes. Sci. Technol.* **2000**, *14*, 43–66. [CrossRef]
27. Mortensen, F.; Thomsen, O.T. Analysis of adhesive bonded joints: A unified approach. *Compos. Sci. Technol.* **2002**, *62*, 1011–1031. [CrossRef]
28. Renton, W.J.; Vinson, J.R. The Efficient Design of Adhesive Bonded Joints. *J. Adhes.* **1975**, *7*, 175–193. [CrossRef]
29. Pascoe, J.A.; Alderliesten, R.C.; Benedictus, R. Methods for the prediction of fatigue delamination growth in composites and adhesive bonds—A critical review. *Eng. Fract. Mech.* **2013**, *112–113*, 72–96. [CrossRef]
30. Srinivas, S. *Analysis of Bonded Joints NASA Technical Note*; NASA Langley Research Center: Hampton, VA, USA, 1975.
31. Allman, D.J. A theory for elastic stresses in adhesive bonded lap joints. *Q. J. Mech. Appl. Math.* **1977**, *30*, 415–436. [CrossRef]
32. Ojalvo, I.U.; Eidinoff, H.L. Bond thickness effects upon stresses in single-lap adhesive joints. *AIAA J.* **1978**, *16*, 204–211. [CrossRef]
33. Delale, F.; Erdogan, F.; Aydinoglu, M.N. Stresses in Adhesively Bonded Joints: A Closed-Form Solution. *J. Compos. Mater.* **1981**, *15*, 249–271. [CrossRef]
34. Bigwood, D.A.; Crocombe, A.D. Elastic analysis and engineering design formulae for bonded joints. *Int. J. Adhes. Adhes.* **1989**, *9*, 229–242. [CrossRef]
35. Cheng, S.; Chen, D.; Shi, Y. Analysis of AdhesiveBonded Joints with Nonidentical Adherends. *J. Eng. Mech.* **1991**, *117*, 605–623. [CrossRef]
36. Dillard, D.A. *Applying Fracture Mechanics to Adhesive Bonds*; Woodhead Publishing: Cambridge, UK, 2021; ISBN 9780128199541.
37. Lyathakula, K.R.; Yuan, F.G. A probabilistic fatigue life prediction for adhesively bonded joints via ANNs-based hybrid model. *Int. J. Fatigue* **2021**, *151*, 106352. [CrossRef]
38. Reddy Lyathakula, K.; Yuan Karthik Reddy Lyathakula, F.-G.; Yuan, F.-G. Probabilistic fatigue life prediction for adhesively bonded joints via surrogate model. In Proceedings of the Sensors and Smart Structures Technologies for Civil, Mechanical, and Aerospace Systems 2021, Online, 22 March 2021; Volume 11591, pp. 152–162. [CrossRef]
39. Akhavan-Safar, A.; Marques, E.A.S.; Carbas, R.J.C.; da Silva, L.F.M. *Cohesive Zone Modelling for Fatigue Life Analysis of Adhesive Joints*; Springer Briefs in Applied Sciences and Technology; Springer International Publishing: Cham, Switzerland, 2022; ISBN 978-3-030-93141-4.
40. Zhang, L.; Dong, P.; Wang, Y.; Mei, J. A Coarse-Mesh hybrid structural stress method for fatigue evaluation of Spot-Welded structures. *Int. J. Fatigue* **2022**, *164*, 107109. [CrossRef]
41. Kanninen, M.F. An augmented double cantilever beam model for studying crack propagation and arrest. *Int. J. Fract.* **1973**, *9*, 83–92. [CrossRef]
42. Mei, J.; Dong, P.; Kalnaus, S.; Jiang, Y.; Wei, Z. A path-dependent fatigue crack propagation model under non-proportional modes I and III loading conditions. *Eng. Fract. Mech.* **2017**, *182*, 202–214. [CrossRef]
43. Rybicki, E.F.; Kanninen, M.F. A finite element calculation of stress intensity factors by a modified crack closure integral. *Eng. Fract. Mech.* **1977**, *9*, 931–938. [CrossRef]
44. Dong, P. A structural stress definition and numerical implementation for fatigue analysis of welded joints. *Int. J. Fatigue* **2001**, *23*, 865–876. [CrossRef]
45. Dong, P. A robust structural stress procedure for characterizing fatigue behavior of welded joints. *SAE Tech. Pap.* **2001**, *110*, 89–100. [CrossRef]
46. Dong, P. A Robust Structural Stress Method for Fatigue Analysis of Offshore/Marine Structures. *J. Offshore Mech. Arct. Eng.* **2005**, *127*, 68–74. [CrossRef]